Journal of Materials Chemistry C

ROYAL SOCIETY OF CHEMISTRY

PAPER

View Article Online
View Journal

Published on 02 September 2022. Downloaded by UNIV DEGLI STUDI DI CAGLIARI on 9/21/2022 10:52:37 AM.

Check for updates

Cite this: DOI: 10.1039/d2tc02919g

White light emission with unity efficiency from $Cs_2Na_{1-x}Ag_xIn_{1-y}Bi_yCl_6$ double perovskites: the role of bismuth and silver†

Fang Liu,[a] Angelica Simbula,[a] Stefano Lai,[a] Luyan Wu,[a] Qingqian Wang,[b] Daniela Marongiu,*[a] Riccardo Pau,[ac] Selene Matta,[a] Federico Pitzalis,[a] Alessandra Geddo Lehmann,[a] Kai Wang,[b] Alessio Filippetti,[ad] Francesco Quochi,*[a] Michele Saba,[a] Andrea Mura[a] and Giovanni Bongiovanni[a]

Double perovskites $Cs_2Na_{1-x}Ag_xIn_{1-y}Bi_yCl_6$ can emit warm white light with almost unity quantum efficiency and are thus among the most promising materials for solid-state lighting. The emission spectrum is reproducible and the materials themselves are robust against degradation, as well as fabricated from earth-abundant, non-toxic precursors. The emission efficiency is however sensitive to the materials composition, with small variations modifying the photoluminescence quantum yield by more than an order of magnitude. We provide here a comprehensive, systematic study of the optical properties as a function of composition and identify the microscopic mechanism linking the presence of Bi and Ag to the high emission quantum yield. A 0.1% minimum fraction of Bi and Ag is found to trigger efficient emission of warm white light. Ag alloying is fundamental to obtain high emission yields. Continuous-wave spectroscopy measurements are complemented with *ab initio* computation of the electronic band structure in demonstrating that Bi strengthens optical absorption at the band gap edge of the double perovskites. In addition, it is found by combining time-resolved photoluminescence and transient absorption spectroscopy that Ag and Bi promote the formation of bright (radiative) self-trapped excitons, while inhibiting exciton relaxation into long-lived dark states.

Received 11th July 2022,
Accepted 2nd September 2022

DOI: 10.1039/d2tc02919g

rsc.li/materials-c

Introduction

Solid-state lighting requires materials to emit white light, comfortable for the human eye and capable of faithfully rendering colors. Color conversion schemes and mixtures of multiple emitters have been deployed,[1] plagued however by issues such self-absorption and poor color rendering index.[2] Single-component white light emitting materials are most desirable, especially with high emission efficiency and the right spectrum. Recently, halide perovskites with various structural dimensionality (0D,[3,4] 1D,[5] 2D[6,7] and 3D[8–11]) have been reported to emit broadband white light, with high efficiency and negligible reabsorption. Among the proposed materials compositions, double perovskites $Cs_2Na_{1-x}Ag_xIn_{1-y}Bi_yCl_6$ are the most successful realization of warm white light emitters.[8,12–23] Such compounds are typically transparent in the visible range, with bandgaps between 300 nm and 400 nm, depending on the exact composition. The emission spectrum is centered around 550–600 nm and over 200 nm wide, almost covering the whole visible spectrum, with the main weight on the red part, producing a warm white continuum. The optical emission mechanism has been linked to self-trapped excitons (STEs), since in halide perovskites charge carriers can couple to a soft lattice, inducing transient deformation of the crystal lattice and are thus localized.[24–28] The broadband emission with large Stokes shift is then caused by lattice distortion in the excited state with respect to the ground state.[14,29–33] Warm white light emission appears therefore as a general and robust phenomenon in a wide variety of materials compositions, even with different bandgaps and optical absorption properties.[34,35]

The emission efficiency however varies wildly according to composition. Among the most prominent examples, in

[a] Dipartimento di Fisica, Università degli Studi di Cagliari, Monserrato (CA), I-09042, Italy. E-mail: daniela.marongiu@dsf.unica.it, quochi@unica.it
[b] Department of Electrical and Electronic Engineering, Southern University of Science and Technology, Shenzhen, 518055, China
[c] Zernike Institute for Advanced Materials, University of Groningen, Nijenborgh 4, 09747 AG Groningen, The Netherlands
[d] Istituto Officina dei Materiali (CNR-IOM) Cagliari, Monserrato (CA), I-09042, Italy

† Electronic supplementary information (ESI) available: Additional structural, Raman and photoluminescence data, and additional *ab initio* calculations. See DOI: https://doi.org/10.1039/d2tc02919g

Published on 02 September 2022. Downloaded by UNIV DEGLI STUDI DI CAGLIARI on 9/21/2022 10:52:37 AM.

$Cs_2Na_{1-x}Ag_xInCl_6$ the substitution of a small fraction of In atoms with Bi causes the emission efficiency to increase by over an order of magnitude and to approach unity;[12,36] whether Bi atoms cure extrinsic defects or provide natural recombination centers is still a wide-open question. Similarly, in $Cs_2NaBiCl_6$ the addition of Ag boosts emission efficiency by a very large factor, an effect that has been linked to parity breaking in valence band orbitals, increasing the oscillator strength of the interband optical transitions.[12]

A comprehensive understanding of the microscopic mechanisms producing the rules for efficient emission is still an open question. We provide here a systematic study of the role of Ag substitution in $Cs_2NaIn_{1-y}Bi_yCl_6$ and Bi substitution in $Cs_2Na_{1-x}Ag_xInCl_6$ as a function of the substitution fraction. Photoluminescence quantum yield (PLQY) measurements are complemented with photoluminescence excitation (PLE), Raman spectroscopy and ultrafast spectroscopy in the form of differential transmission (DT/T) and time-resolved photoluminescence (TRPL). Results are interpreted in the light of theoretical *ab initio* calculations of the electronic structure based on the variational pseudo-self-interaction corrected (VPSIC) approach,[37] highlighting the role of Bi and Ag substitution in the double perovskite structure.

Experimental section

Chemicals

Cesium chloride (CsCl, 99.999%), silver nitrate ($AgNO_3$, 99.9%), indium oxide (In_2O_3, 99.95%), and hydrochloric acid (HCl, 36%) were purchased from Alfa Aesar. Sodium chloride (NaCl, >99%), and bismuth oxide (Bi_2O_3, 99.9%) were purchased from Sigma Aldrich. Potassium chloride (KCl, >99.5%) was purchased from Merck & Co. AgCl was precipitated from as prepared aqueous solutions of $AgNO_3$ and KCl.

Synthesis of alloyed $Cs_2Na_{1-x}Ag_xInCl_6$ double-perovskite crystals

Single crystals of double perovskite $Cs_2Na_{1-x}Ag_xInCl_6$ can be crystallized following the super-saturation precipitation method described in the previous literature[38] while In_2O_3 and Bi_2O_3 were used instead of the chlorine compounds because of their hygroscopicity problem. Briefly, 0.5 mmol In_2O_3 were added in 10 mL HCl solution and stirred under 110 °C until fully dissolved. 2 mmol of CsCl were then added and white precipitate formed immediately. HCl was added until the solution turned to be transparent. Then x mmol of AgCl and $1 - x$ mmol of NaCl were added and white precipitate formed again. The solution started to be heated to 120 °C. More HCl could be added to make all the solids totally dissolved. The solution was held at 120 °C for 2 h. Then the stir bar was removed from the solution before the solution was cooled to room temperature. Crystals with 50–500 μm size formed from solution upon stirring at room temperature overnight. These crystals were filtered with Buchner funnel, washed with ethanol, and dried under reduced pressure overnight. The yield of the obtained product is about 75%. Bi-doped alloyed double perovskite was synthesized by substituting the In_2O_3 with a mixture of 0.495 mmol In_2O_3 and 0.005 mmol Bi_2O_3 in 10 mL HCl solution, followed by the same procedure as for the $Cs_2Na_{1-x}Ag_xInCl_6$ synthesis.

Synthesis of alloyed $Cs_2NaIn_{1-y}Bi_yCl_6$ double-perovskite crystals

A mixture of $0.5 \times (1 - y)$ mmol In_2O_3 and $0.5 \times y$ mmol Bi_2O_3 were added in 10 mL HCl solution and stirred under 110 °C until fully dissolved. 2 mmol of CsCl were then added and white precipitate formed immediately. HCl was added until the solution turned to be transparent. Then 1 mmol NaCl was added, and the solution started to be heated to 120 °C. More HCl could be added to make the solids totally dissolved. The solution was held at 120 °C for 2 h. Crystals ranging in size from 100 μm to 1 mm formed from solution upon stirring at room temperature overnight. These crystals were filtered with Buchner funnel, washed with ethanol, and dried under reduced pressure overnight. Ag-doped alloyed double perovskite was synthesized by substituting NaCl with a mixture of 0.99 mmol NaCl and 0.01 mmol AgCl, followed by the same procedure as for the $Cs_2NaIn_{1-y}Bi_yCl_6$ synthesis.

Materials characterization

X-ray diffraction (XRD) measurements were conducted by a powder diffractometer (D8 ADVANCE, Bruker) using a Cu Kα radiation, and the acquisition was done with 0.04° step size over the 2 theta angle range of 10°–65°. The crystals were finely ground in a mortar before characterization. Raman spectroscopy experiments were performed in back-scattered geometry with a micro-Raman OEM system. The emission at 785 nm from a fiber-coupled laser diode (BWTEK BRM-785) was focused onto the samples by means of a 10× microscope objective (laser spot diameter on the sample ~200 μm). Raman signals were recorded by a fiber-coupled grating spectrometer coupled with a thermoelectrically cooled CCD (BWTEK BTC667N-785S) with spectral resolution better than 5 cm^{-1}. The Rayleigh scattering was rejected by means of an edge-filter cutting at nearly 65 cm^{-1}. The laser power was kept below 3 mW to avoid sample damage. PLQY measurements were performed at room temperature using an absolute PL spectrometer (Hamamatsu Quantaurus-QY C11347-11). PLE measurements were performed at the emission wavelength of 650 nm with 1 (2) nm bandwidth in excitation (detection) using a Horiba Fluoromax-4 spectrofluorometer. Elemental analysis was carried out *via* Inductively Coupled Plasma Optical Emission Spectrometry (ICP-OES) with Agilent 5110. For the analyses, 70–100 μg of the sample were subsequently dissolved in 6.5 mL of hydrochloric acid (HCl, GR, 36–38%, v/v), then the solution transferred to a 25 mL volumetric flask, and diluted with ultra-pure water to volume. Standard solutions (0, 1, 3, 5, 10 mg L^{-1}) were used to perform elemental calibration curves. All measurements were done setting the instrument with the following parameters: plasma power 1200 W; plasma flow 12 L min^{-1}; auxiliary flow 1 L min^{-1}; pump rate 12 rpm.

 This journal is © The Royal Society of Chemistry 2022

Published on 02 September 2022. Downloaded by UNIV DEGLI STUDI DI CAGLIARI on 9/21/2022 10:52:37 AM.

Ultrafast optical spectroscopy

Samples were excited with ultrashort laser pulses (100 fs) generated by a titanium:sapphire regenerative amplifier (Coherent Libra) with repetition rate 1 kHz, then converted to excitation wavelength of 360 nm with an optical parametric amplifier (Light Conversion Topas 800). DT/T measurements were performed by probing the samples with ultrafast white pulses at different time delays with respect to the pump pulses, in a differential configuration where a transmitted beam and a reference beam are sent to two distinct CMOS spectrometers with 1 nm spectral resolution. The relative delay was controlled with EOS module from Ultrafast Systems, with time resolution of 1 ps and available time range of 100 μs. Custom modifications to the setup allowed to collect photoluminescence emitted from the same area probed with DT/T technique, in what we call tandem configuration. The PL signal collected is then spectrally dispersed with a grating spectrometer (Acton 2300i), coupled with a streak camera by Hamamatsu (model C10910), resulting in TRPL measurements with sub-ns time resolution (around 100 ps for the shorter time range).

Results and discussion

Materials and structural properties

Crystals of double perovskites $Cs_2Na_{1-x}Ag_xIn_{1-y}Bi_yCl_6$ ($0 \leq x \leq 1$, $0 \leq y \leq 1$) were grown through crystallization in thermal supersaturated solution, a simple and reproducible method. All the double perovskite compositions have highly symmetric face-centered cubic structures (space group $Fm\bar{3}m$), consisting of a 3D framework of corner-connected octahedra $[MCl_6]^{5-}$ or $[M'Cl_6]^{3-}$ (M = Ag^+ or Na^+; M′ = Bi^{3+} or In^{3+}), with Cs^+ ions occupying the octahedral external cavities in the framework. As observed from XRD patterns of two series of compositions $Cs_2Na_{1-x}Ag_xInCl_6$ and $Cs_2NaIn_{1-y}Bi_yCl_6$ (Fig. 1), Na/Ag and In/Bi are incorporated uniformly into the double perovskite, without phase separation or discernible impurities. The intensity of the (111) peak at 14.6° increased with increasing Na amount from 0 to 100% in Fig. 1a confirmed that compounds are alloys. The ionic radius of Na^+ (1.02 Å) is smaller than that of Ag^+ (1.15 Å), however, the bond length of Na–Cl is longer than that of Ag–Cl. Thus, lattice expansion can be observed from the shift of the (422) diffraction peak in Fig. 1b as Na amount is increased.[39] Similarly, with increasing Bi content in $Cs_2NaIn_{1-y}Bi_yCl_6$, the (220) reflection (Fig. 1e) is sequentially shifted to lower 2θ values, indicating the formation of alloyed In/Bi compounds.

The accurate Na/Ag and In/Bi compositional ratios in the final products were obtained using the ICP-OES technique. The unit cell lattice parameter was extracted by Rietveld analysis with the software MAUD (Table S1, ESI†).[40] As shown in Fig. 1c and f, the refined lattice parameter linearly increases upon Na and Bi substitution respectively, supporting the hypothesis of uniform incorporation of substitution elements in the crystal structure. Same results were obtained for In substitution with Bi and Na substitution with Ag at 1% level (Fig. S1, ESI†). The refinement results of all the compounds can be found in Fig. S2 (ESI†).

Raman spectroscopy showed high sensitivity to compositional changes in all double perovskite alloys. Spectra of $Cs_2Na_{1-x}Ag_xInCl_6$ ($0 \leq x \leq 1$) and $Cs_2NaIn_{1-y}Bi_yCl_6$ ($0 \leq y \leq 1$) compounds are reported in Fig. 2. Following literature,[25,28,41–43] the observed peaks were assigned to breathing (T_{2g}) and stretching (E_g, A_{1g}) modes of $[MCl_6]^{5-}$ and $[M'Cl_6]^{3-}$ octahedra. In the $Cs_2Na_{1-x}Ag_xInCl_6$ series (Fig. 2a), both $[AgCl_6]^{5-}$ and $[InCl_6]^{3-}$ octahedra are supposed to contribute to the three modes, as Ag and In have similar elemental properties, while the T_{2g}/A_{1g} intensity ratio increases with

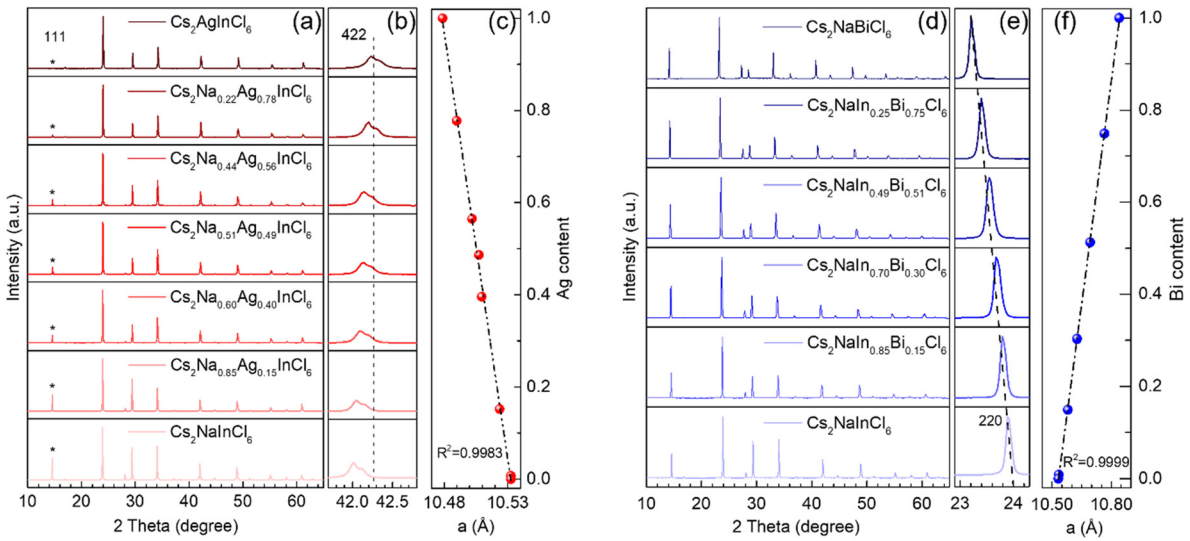

Fig. 1 (a) XRD patterns of $Cs_2Na_{1-x}Ag_xInCl_6$ with different Na/Ag ratio; the asterisks mark the (111) diffraction peak. (b) Enlarged view of (422) diffraction peak shift. (c) Cubic crystal lattice parameter as a function of Ag content. The black dash line shows a Vegard's law fit. (d) XRD patterns of $Cs_2NaIn_{1-y}Bi_yCl_6$ with different In/Bi ratio. (e) Enlarged view of (220) diffraction peak shift. (f) Cubic crystal lattice parameter as a function of Bi content.

Published on 02 September 2022. Downloaded by UNIV DEGLI STUDI DI CAGLIARI on 9/21/2022 10:52:37 AM.

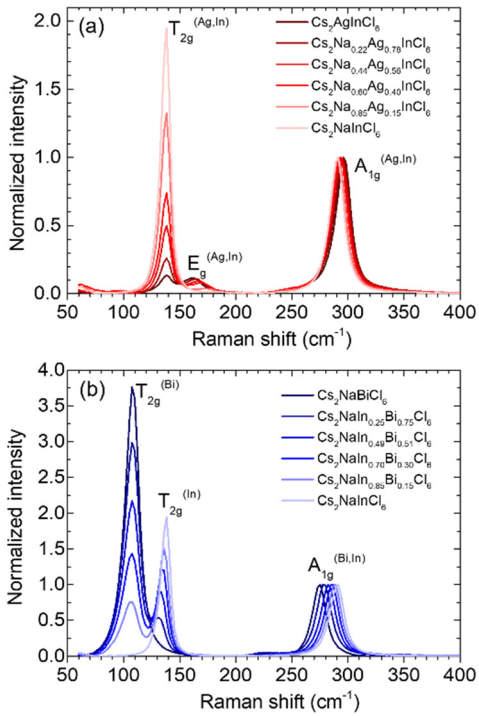

Fig. 2 Raman spectra of (a) $Cs_2Na_{1-x}Ag_xInCl_6$ compounds with different Na/Ag ratios and (b) $Cs_2NaIn_{1-y}Bi_yCl_6$ compounds with different In/Bi ratios. Raman transitions are assigned to vibrational modes of $[MCl_6]^{5-}$ and $[M'Cl_6]^{3-}$ octahedra (see text for details); $M^+/[M']^{3+}$ metal cations relating to each mode are indicated as superscripts in brackets. All spectra are normalized to the intensity of the A_{1g} mode.

increasing Na content, allegedly due to progressive improvement of the crystal lattice quality.[42] Incremental substitution of In with Bi was clearly detected by (i) the decrease in intensity, together with the shift to lower wavenumbers, of the T_{2g} $[InCl_6]^{3-}$ breathing mode, initially located at 138 cm^{-1}, (ii) the complementary rise of the corresponding T_{2g} $[BiCl_6]^{3-}$ mode at 108 cm^{-1}, and (iii) the shift of the A_{1g} stretching mode from 291 to 275 cm^{-1} (Fig. 2b). Overall, we conclude that Ag, In and Bi are all involved in the A_{1g} peak across the 260–300 cm^{-1} region, with Bi mostly contributing to the low-wavenumber tail of the mode (see also Fig. S3, ESI†).[41]

Optical properties

As observed in PL spectra (Fig. 3), $Cs_2Na_{1-x}Ag_xIn_{1-y}Bi_yCl_6$ produced broadband emission, ranging from 400 nm to beyond 900 nm, which could be assigned to STE-based emission. Due to the same even parity of the valence band maximum and conduction band minimum at the Γ point,[21,44–47] the dipole transitions between the band edge states of $Cs_2AgInCl_6$ are parity-forbidden which causes poor band-edge absorption and extremely low PLQY. The emission efficiency was enhanced when Na was alloyed with Ag, with the highest value of 12% for an Ag content $x = 0.78$. The second PLQY relative maximum located at $x = 0.4$ could in part be traced back to batch-to-batch fluctuations possibly arising from irreproducible extrinsic effects, such as different concentrations of structural defects/electronic traps, in double perovskites with almost identical elemental compositions and crystal structures. Furthermore, the addition of a small Bi fraction, namely 1%, significantly enhances the emission efficiency without significantly affecting the crystal structure (Fig. S1a–c, ESI†). The PLQY of $Cs_2Na_{1-x}Ag_xIn_{0.99}Bi_{0.01}Cl_6$ compound reaches 97% for the composition with Ag content $x = 0.39$ (Fig. 3c, red spheres). This should be contrasted with the results reported in ref. 12, where the PLQY maximum is reached at $x \sim 0.6$. We argue that different synthetic protocols can result in double perovskites with different excited-state and photophysical properties, including exciton self-trapping efficiency and radiative efficiency, which both contribute to the PLQY. Starting from the $Cs_2NaInCl_6$ perovskite, again very low PLQY values were measured when only Na was kept as the monovalent cation, and In and Bi were alloyed as the trivalent cations. However, the addition of 1% Ag activated efficient emission (Fig. 3d, red spheres), while keeping the crystal structure unaltered (Fig. S1d–f, ESI†). The emission spectrum of $Cs_2Na_{0.99}Ag_{0.01}In_{1-y}Bi_yCl_6$ shows a redshift that increases for increasing Bi content; this is tentatively ascribed to a progressive increase in exciton self-trapping energy not counterbalanced by a band-gap renormalization (see PL/PLE spectra along with peak PL/PLE photon energies in Fig. S4 in the ESI†).

Bi and Ag both play an important role for achieving highly efficient warm white light emission from $Cs_2Na_{1-x}Ag_xIn_{1-y}Bi_yCl_6$ compounds. To quantify the minimum amount needed to trigger efficient emission, systematic analyses were first performed with incremental concentrations of Bi, starting from the $Cs_2Na_{0.6}Ag_{0.4}InCl_6$ composition. Fig. 4a and b shows PL and PLE spectra, and PLQY values for the series of materials compositions. The minimum amount of Bi needed to activate efficient radiative recombination appears to be around 0.1%. Correspondingly, a new absorption peak appears in the PLE spectrum around 350 nm, lower in energy than the 275 nm maximum in the Bi-free compound, and grows in intensity with increasing Bi concentration. The highest PLQY value was reached for 1% Bi alloying, whereas further increasing of Bi content reduced the PLQY, possibly because of self-quenching effects.[48] Saturation effects in optical absorption are also visible at the highest Bi fractional abundances. A parallel study was conducted on $Cs_2NaBiCl_6$ alloyed with incremental amounts of Ag (Fig. 4c and d). Again, the minimum amount of Ag needed to activate the efficient emission is about 0.1%.

In the case of Ag alloying, however, no new peak appears in the PLE spectra; only a progressive broadening of the two main spectral features is observed with increasing Ag content. Raman spectra relating to materials compositions shown in Fig. 4 are reported in Fig. S3 (ESI†).

Theory of electronic band structure

As well known, standard Density Functional Theory (DFT) based on local functionals largely fails at a sufficiently accurate description of the band structure; for a correct interpretation of the measurements, it is instrumental to use an advanced, beyond-local functional capable to correct the main DFT

 This journal is © The Royal Society of Chemistry 2022

Published on 02 September 2022. Downloaded by UNIV DEGLI STUDI DI CAGLIARI on 9/21/2022 10:52:37 AM.

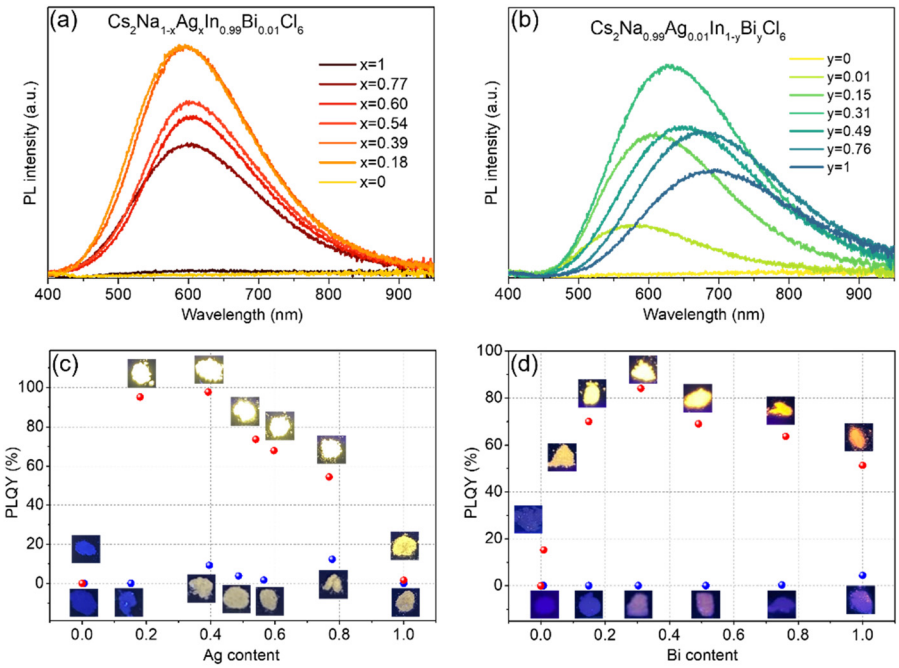

Fig. 3 (a) PL spectra of $Cs_2Na_{1-x}Ag_xIn_{0.99}Bi_{0.01}Cl_6$ compounds under 365 nm continuous-wave photoexcitation. (b) Same as (a) but for $Cs_2Na_{0.99}Ag_{0.01}In_{1-y}Bi_yCl_6$ compounds. (c) PLQY of both $Cs_2Na_{1-x}Ag_xInCl_6$ (blue spheres) and $Cs_2Na_{1-x}Ag_xIn_{0.99}Bi_{0.01}Cl_6$ (red spheres), photoexcited at 365 nm, as a function of Ag content. (d) Same as (c) but for $Cs_2NaIn_{1-y}Bi_yCl_6$ and $Cs_2Na_{0.99}Ag_{0.01}In_{1-y}Bi_yCl_6$ as a function of Bi content. Inset photos depict corresponding samples under UV photoexcitation within the 330–360 nm spectral band.

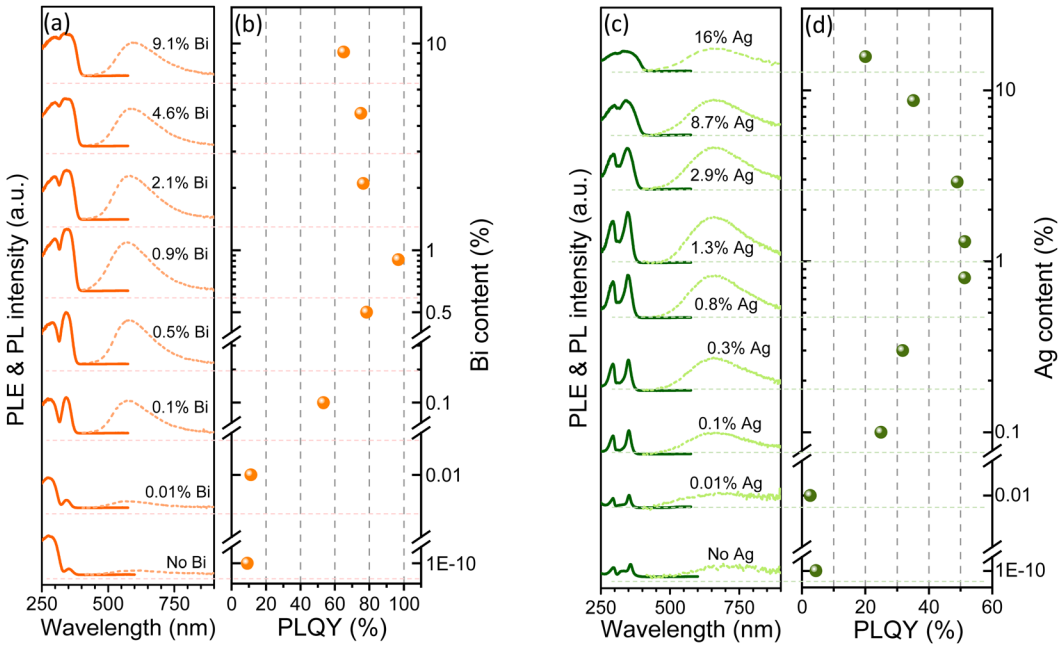

Fig. 4 (a) PLE spectra (solid lines) and PL spectra (dashed lines); (b) PLQY of $Cs_2Na_{0.6}Ag_{0.4}InCl_6$ compounds alloyed with Bi, photoexcited at 365 nm wavelength. (c and d) Same as (a and b) but for $Cs_2NaBiCl_6$ alloyed with Ag.

deficiencies. The VPSIC approach,[37] based on the removal of the spurious self-interaction from the energy functional, is typically accurate for a broad range of materials,[49,50] delivering band gaps within 10% from the measured values, and yet, it is much less computationally demanding than other popular beyond-DFT methods such as HSE06 or GW. In particular, a self-interaction free approach is instrumental to the prediction of accurate electronic defect energies.[51] In the past the VPSIC

Published on 02 September 2022. Downloaded by UNIV DEGLI STUDI DI CAGLIARI on 9/21/2022 10:52:37 AM.

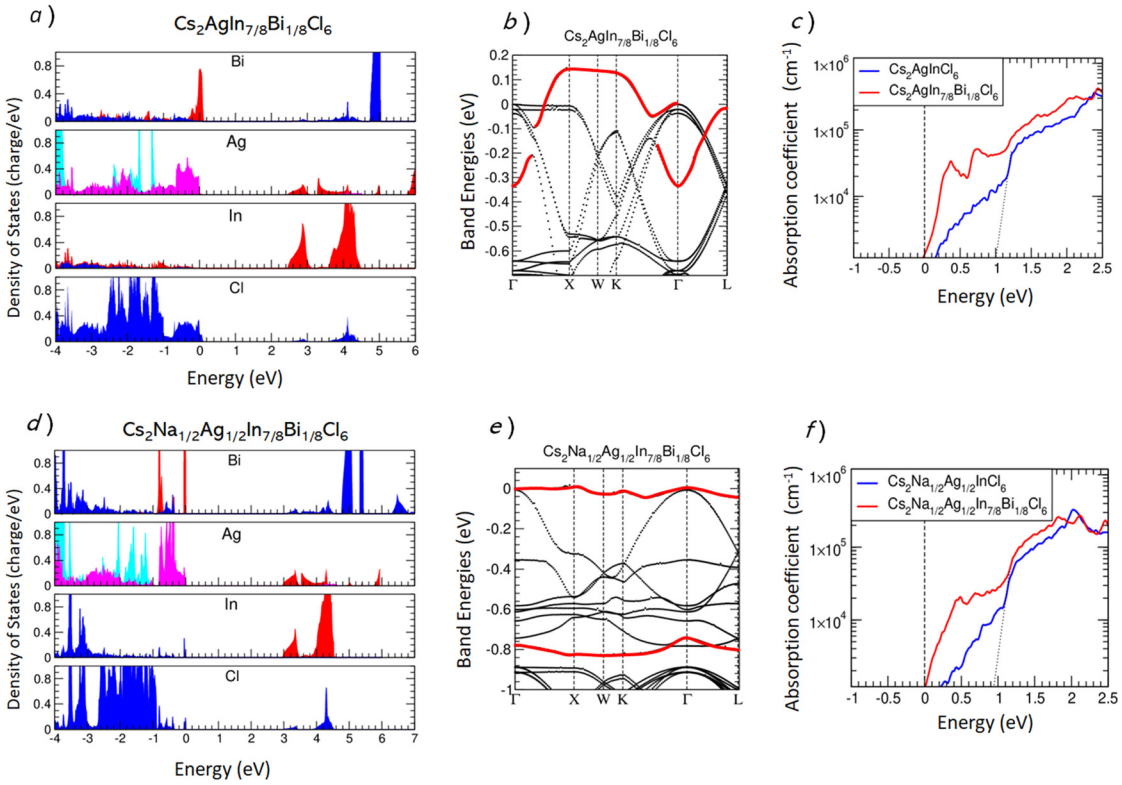

Fig. 5 DOS, band energies, and absorption spectrum calculated for some representative double perovskites. (a) Orbital-resolved DOS for $Cs_2AgIn_{7/8}Bi_{1/8}Cl_6$; different colors are used for different orbital contributions: s (red), p (blue), e_g (magenta), t_{2g} (cyan); zero energy is fixed to the VBM. (b) Band energies in the region nearby the VBM; the red band derives from the fully occupied Bi 6s states introduced by In substitutions with Bi, and corresponds to the s peak of the same color visible in the Bi DOS (upmost panel a). (c) Absorption spectra for the compound with and without In substitution with Bi; here zero energy is fixed at the band gap of the corresponding material. Red lines are for Bi compounds; the dotted lines extrapolate the 'optical gap', *i.e.*, the region where optical transitions are strongly suppressed due to parity symmetry; we see that the Bi presence largely relaxes the parity-forbidden condition. (d–f) Same as (a–c) for host material $Cs_2Na_{1/2}Ag_{1/2}InCl_6$; the Na DOS is not included since largely discardable in this energy range.

was used to describe $Cs_2AgInCl_6$ and $Cs_2AgInBr_6$;[46] here we apply the VPSIC to analyze $Cs_2Na_{1-x}Ag_xIn_{1-y}Bi_yCl_6$ for several x and y compositions, simulated using 80-atom fcc supercells. The lattice parameters of the pristine $Cs_2NaInCl_6$ and $Cs_2AgInCl_6$ compounds were determined by VPSIC optimization and the values, 10.51 Å and 10.39 Å, respectively, were found in satisfactory agreement with the experimental results.

We start from the analysis of Bi doping in $Cs_2AgInCl_6$ by comparing orbital-resolved density of states (DOS) and band energies of $Cs_2AgInCl_6$ and $Cs_2AgIn_{7/8}Bi_{1/8}Cl_6$ (Fig. 5a): $Cs_2AgInCl_6$ is an insulator with direct band gap at Γ point of 2.14 eV which opens between In 5s states at CBM and Ag 4d states at VBM (the optical gap is however much larger due to parity forbidden transitions, see *e.g.* ref. 46 for a detailed explanation). In substitution with Bi produces a dramatic change in the band structure, namely the inclusion of a fully occupied, double-degenerate 6s band, whose top side is located 0.14 eV above the host material VBT; the Bi 6s orbitals, however, are rather spread in space, and overlap significantly with Ag 4d e_g, and Cl 3p states; this causes a 6s band dispersion of 0.48 eV. Theoretical arguments[51] show that, in the low-concentration limit, the BZ-averaged electronic energy (which is 20 meV above the VBM) approximates the energy of the fully localized point defect. On the other hand, the empty Bi 6p states are peaked way above ($\sim$2.5 eV higher than) the CBM, thus they are unlikely to play any significant role in optical emission. According to our calculations, the presence of Bi induces a remarkable enhancement of the absorption rate (Fig. 5c); this effect is evident in the 1 eV energy region above the CBM, where the $Cs_2AgInCl_6$ absorption is largely parity-forbidden, while with Bi doping, a $\sim 5 \times 10^4$ cm^{-1} absorption peak is obtained. The parity-forbidden condition is overcome since the Bi 6s band (Fig. 5b) contributes to the absorption all over the BZ, and not mainly at the Γ point, like the Ag e_g bands which dominate the VBM of the host material.

We reach similar conclusions concerning Bi doping even for the host material $Cs_2NaInCl_6$, a wide-gap insulator with direct band gap of 4.6 eV (results are shown in ESI†): In–Bi substitution introduces a fully occupied 6s band well within the host material band gap; in absence of Ag 4d states, the Bi 6s orbitals are much more localized in space and the corresponding band much flatter. The 6s band generates an absorption peak of $\sim 10^4$ cm^{-1} for energies lower than the host material band gap (Fig. 5c).

Finally, we analyze the Ag/Na mixing; the band gap is extremely sensitive to this mixing for two reasons: first, Ag 4d

 This journal is © The Royal Society of Chemistry 2022

Published on 02 September 2022. Downloaded by UNIV DEGLI STUDI DI CAGLIARI on 9/21/2022 10:52:37 AM.

states dominate the VBM, thus the Ag–Na substitution pushes the VBM progressively down in energy; second, the loss of Ag 5s–In 5s hybridization causes the collapse of In 5s bandwidth, and a corresponding increase of the CBM. These combined effects result in the ∼2 eV band gap difference between pure Na and Ag compounds (see ESI† for details). For what concerns In–Bi substitutions, in Fig. 5d–f we compare $Cs_2Na_{1/2}Ag_{1/2}InCl_6$ and $Cs_2Na_{1/2}Ag_{1/2}In_{7/8}Bi_{1/8}Cl_6$; the host material has a direct band gap at Γ point of 2.8 eV, but the absorption rate is largely suppressed by parity-forbidden symmetry up to 3.8 eV; with In–Bi substitutions, a Bi 6s peak appears just at the VBM, partially hybridized with the Cl 3p states; in Fig. 5d, a second peak derived from 6s states is present at lower energy, resulting from the hybridization with Ag e_g states. Once again, the Bi inclusion relaxes the parity-forbidden condition and restores a significant absorption right above the band gap edge.

Overall, the VPSIC simulations unveil the crucial role played by Bi in the optical properties: In–Bi substitutions represent, in all the examined cases, strong absorption centers, whose chemical mechanism is based on the presence of filled Bi 6s in-gap electronic states located just above the VBT of the host; In–Bi substitutions also introduce empty Bi 6p states in the conduction bands, but they are too high in energy to give a significant contribution at the onset, even for a remarkably large Bi concentration. For what concerns Ag, calculations do not evidence a significant role in the enhancement of the absorption rate, suggesting that the crucial role of Ag observed in optical emission is likely due to the Ag self-trapping polaronic behavior, which is not included in our theoretical treatment.

Time dynamics of optical excitations

Ultrafast spectroscopy with femtosecond laser pulses was employed to investigate the dynamics of optical excitations, particularly the formation of STEs and their decay times. TRPL tracks directly the radiative recombination of STEs. DT/T technique in a pump-probe configuration was also employed, yielding complementary information to TRPL decays.[52] DT/T is a proxy for transient absorption and detects modifications in the absorption spectrum of a weak, broadband probe pulse induced by the presence of the optical excitations injected by an intense ultraviolet pump pulse. Probe light propagates through the mm-thick crystals (Fig. S7, ESI†) and the portion of spectrum with photon energies above the bandgap is not transmitted, since the characteristic absorption length is much less than 1 mm; therefore, no bleaching signal resonant with the band-to-band absorption onset can be observed in transmission geometry. The DT/T signal in double perovskites appears instead as photoinduced absorption in the visible spectrum, at photon energies below the bandgap, as reported in Fig. 6. The photoinduced absorption spectrum range is roughly the same as that of the PL emission (Fig. 6c and f), and we attribute it to excited-state absorption. Results obtained in $Cs_2Na_{0.6}Ag_{0.4}In_{1-y}Bi_yCl_6$ (y = 0, ∼0.01) and in $Cs_2Na_{1-x}Ag_xBiCl_6$ (x = 0, ∼0.01) highlight the effect of Bi and Ag substitutions on the excited-state dynamics of the double perovskites. In these compounds, elemental substitution at the 1% level resulted in a ten-fold increase in PLQY (Fig. 3c and d), which achieves a value of 50% and 100% in $Cs_2Na_{0.99}Ag_{0.01}BiCl_6$ and $Cs_2Na_{0.6}Ag_{0.4}In_{0.99}Bi_{0.01}Cl_6$, respectively.

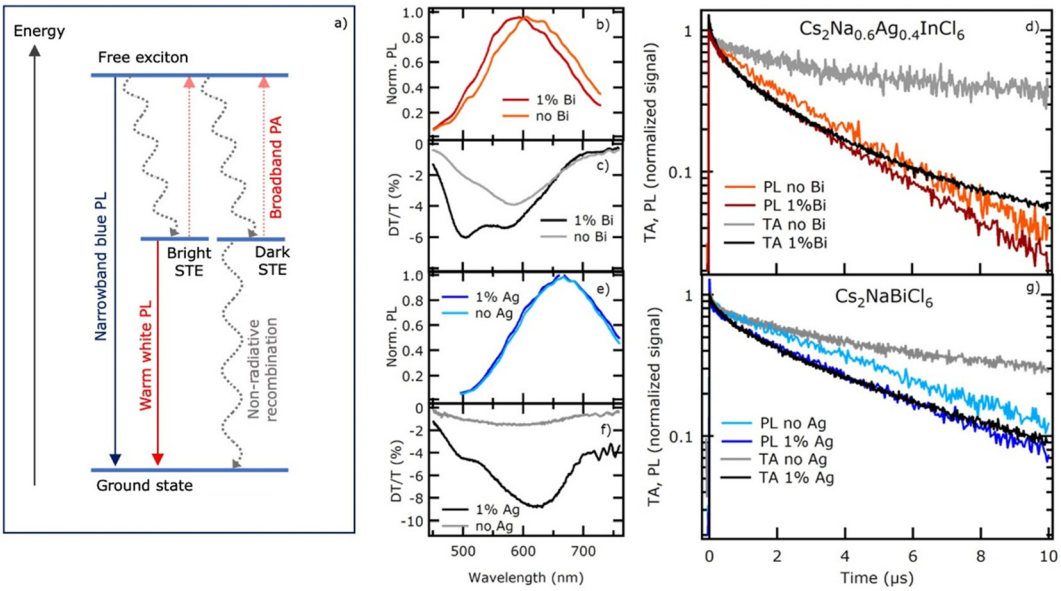

Fig. 6 (a) Sketch of the ground state and excited states of the double perovskite illustrating the physical origin of warm white light emission and photoinduced absorption. On the right side, TRPL and DT/T spectra and time profiles for $Cs_2Na_{0.6}Ag_{0.4}InCl_6$ with partial Bi substitution (b–d), and $Cs_2NaBiCl_6$ with partial Ag substitution (e–g). Photoinduced absorption signals, appearing as negative DT/T spectra (c and f), were taken positive (TA = DT/T) for an easier visualization of the decay profiles (d and g).

Published on 02 September 2022. Downloaded by UNIV DEGLI STUDI DI CAGLIARI on 9/21/2022 10:52:37 AM.

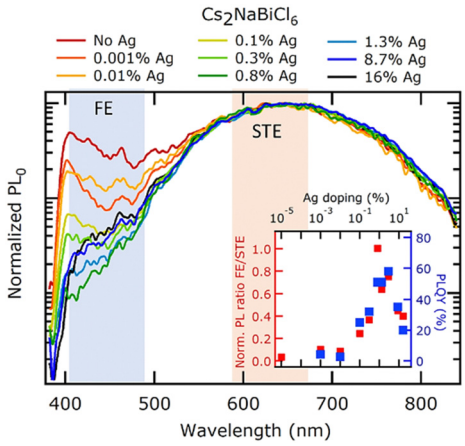

Fig. 7 PL_0 spectra for the $Cs_2NaBiCl_6$ crystals with various amounts of Ag inclusion were taken in a spectral window of 100 ps around the arrival of the excitation pulse. In the inset, the red markers are the ratio of intensities in the FE and STE spectral ranges (integrated in the light-blue and light orange shaded regions respectively) compared with the PLQY (blue markers). The cutoff at 400 nm is due to a drop in the detection setup efficiency.

As shown in Fig. 6d, the DT/T lifetime of $Cs_2Na_{0.6}Ag_{0.4}InCl_6$ is much longer than the PL one, meaning that the majority of excitons are trapped in long-lived dark states. The presence of Bi significantly shortens the DT/T decay making it comparable to the TRPL one, indicating that Bi cures exciton trapping in dark states. Since the TRPL decay is rather insensitive to Bi substitution up to 1% level, bright STEs with nearly 100% radiative efficiency are inferred to exist even in the absence of Bi centers, while their effective formation efficiency upon impulse photoexcitation becomes quantitative at 1% substitution level. Hence, the observed TRPL lifetime practically equals the STE radiative lifetime. The minor variation observed in the DT/T spectrum upon Bi substitution suggests that dark exciton states actually lie close to bright STEs in energy (Fig. 6a). Introduction of Ag in $Cs_2NaBiCl_6$ (Fig. 6g) also produces a shortening of DT/T decay attributed to dark STEs, with the DT/T and TRPL decay profiles nearly overlapping each other over a 10 μs timescale, supporting the conclusion that also Na–Ag substitution makes formation of bright STEs a quantitative process. These results were obtained in a regime of linear response of the double perovskites, where the initial PL signal (PL_0) scales linearly for increasing pump fluence and the TRPL decay is almost insensitive to pump fluence (Fig. S8, ESI†). A DT/T-TRPL comparative study for increasing Bi and Ag contents is reported for completeness in Fig. S9 (ESI†).

Additional information on the formation of bright STEs could be obtained in $Cs_2Na_{1-x}Ag_xBiCl_6$ compounds by a closer inspection into the subnanosecond time scale after photoexcitation for increasing Ag content (Fig. 7). Right after excitation, the emission spectrum of $Cs_2NaBiCl_6$ exhibits two components, the long-lived broadband visible emission from bright STEs and the narrow-band, short lived UV emission ascribed to free excitons (FEs). In the absence of Ag the intensity of the two emission bands is comparable, but the addition of small quantities of Ag to $Cs_2NaBiCl_6$ enhances the visible emission from STEs at the expenses of the FE one. The FE emission almost disappears for an Ag content of 0.5%; further increase of the Ag fraction reduces the warm white light emission efficiency, and therefore the overall PLQY.

The lower inset in Fig. 7 shows the correlation between the initial STE emission intensity (PL_0), with respect to the FE one, and the PLQY. The STE/FE PL_0 ratio and the PLQY follow the same trend as a function of the Ag content, which is compatible with the assumption that the FE emission intensity scales as the absorptance, owing that the emission is almost uniquely contributed by bright STEs. In the TRPL from $Cs_2Na_{0.6}Ag_{0.4}In_{1-y}Bi_yCl_6$ materials on the other hand no evidence of emission from FEs could be observed in the detected wavelength range (see Fig. S10, ESI†).

Conclusions

A systematic investigation of the excited state dynamics in $Cs_2Na_{1-x}Ag_xIn_{1-y}Bi_yCl_6$ double perovskites as a function of materials composition reveals the ingredients for the high quantum efficiency (up to 100%) of the warm white light emission. PLE is interpreted in light of *ab initio* simulations of the band structure, showing that In substitution with Bi introduces lowest-energy band-to-band transitions with large oscillator strength; Na substitution with Ag on the other hand does not change the optical absorption spectrum significantly, apart from a marginal increase in oscillator strength favored by the breaking of parity. PLQY measurements demonstrate that Bi and Ag substitutions at 0.1% levels are sufficient to enhance the PLQY above 20%. Two ultrafast spectroscopy techniques, DT/T and TRPL, were applied in tandem configuration to understand the dynamics of the excited state. Experimental results show that introduction of Bi and Ag suppresses exciton trapping in long-lived dark states in favor of a massive formation of bright STEs, characterized by a nearly radiative-recombination-limited dynamics. An Ag-induced self-trapping polaronic behavior is also suggested as a potential mechanism for formation of bright STEs in high yields. Once Bi and Ag are present in the double perovskite structure, high emission efficiency with a consistent warm white light spectrum arising from bright STEs may occur in a wide variety of materials compositions. Double perovskites realize therefore an almost ideal platform for solid-state lighting.

Author contributions

DM, FQ and MS conceptualized and supervised the research project. FL, AS, SL, QW, DM, FQ and MS performed the experimental investigations and did the formal data analysis. AF performed the theoretical calculations. FL, DM, AF, FQ and MS wrote the original draft. All authors critically reviewed the manuscript. All authors read and approved the final version of the manuscript.

 This journal is © The Royal Society of Chemistry 2022

Published on 02 September 2022. Downloaded by UNIV DEGLI STUDI DI CAGLIARI on 9/21/2022 10:52:37 AM.

Conflicts of interest

There are no conflicts to declare.

Acknowledgements

The authors acknowledge access to research infrastructure in CeSAR—Centro Servizi di Ateneo per la Ricerca at Università degli Studi di Cagliari and thank Dr M. Marceddu and Dr E. Podda for technical assistance. Consorzio AUSI is also acknowledged for financial support through project ''PALFESAE'' (Determina CTS-AUSI del 05/03/2019). A. S. was supported by PON ''Ricerca e Innovazione'' 2014–2020 – Fondo Sociale Europeo, Attraction and International Mobility – AIM1809115-2, Linea 2.1. This work was funded by Regione Autonoma della Sardegna through PO-FSE Sardegna 2007–2013, L. R. 7/2007, ''Progetti di ricerca di base e orientata,'' Projects No. CRP3-114, CRP-17571, CRP-18353, CRP-18013, and CRP-24978, and through Delibera CIPE n. 31 del 20.02.2015 e deliberazione n. 52/36 del 28.10.2015 ''Piano Strategico Sulcis,'' through Project No. SULCIS-820889 and SULCIS-820947, as well as by MUR (Italian Ministry of University and Research) through PRIN 2015 project ''PERovskite-based solar cells: toward high efficiency and long-term stability'' (PERSEO), project number 20155LECAJ. The work was also supported by Fondazione di Sardegna through project 2F20000210007 ''Perovskite materials for photovoltaics.'' A. F. thanks MUR for funding through PRIN 2017 project ''Two-dimensional oxides platform for spin-orbitronics nanotechnology'' (TOPSPIN).

References

1 C. C. Lin and R. S. Liu, *J. Phys. Chem. Lett.*, 2011, **2**, 1268–1277.
2 C. H. Kuo, J. K. Sheu, S. J. Chang, Y. K. Su, L. W. Wu, J. M. Tsai, C. H. Liu and R. K. Wu, *Jpn. J. Appl. Phys., Part 1*, 2003, **42**, 2284–2287.
3 M. B. Teunis, K. N. Lawrence, P. Dutta, A. P. Siegel and R. Sardar, *Nanoscale*, 2016, **8**, 17433–17439.
4 M. Worku, Y. Tian, C. Zhou, S. Lee, Q. Meisner, Y. Zhou and B. Ma, *ACS Appl. Mater. Interfaces*, 2018, **10**, 30051–30057.
5 Z. Yuan, C. Zhou, Y. Tian, Y. Shu, J. Messier, J. C. Wang, L. J. van de Burgt, K. Kountouriotis, Y. Xin, E. Holt, K. Schanze, R. Clark, T. Siegrist and B. Ma, *Nat. Commun.*, 2017, **8**, 14051.
6 M. D. Smith and H. I. Karunadasa, *Acc. Chem. Res.*, 2018, **51**, 619–627.
7 E. R. Dohner, A. Jaffe, L. R. Bradshaw and H. I. Karunadasa, *J. Am. Chem. Soc.*, 2014, **136**, 13154–13157.
8 A. Karmakar, G. M. Bernard, A. Meldrum, A. O. Oliynyk and V. K. Michaelis, *J. Am. Chem. Soc.*, 2020, **142**, 10780–10793.
9 M. Hu, J. Luo, S. Li, J. Liu, J. Li, Z. Tan, G. Niu, Z. Wang and J. Tang, *Opt. Lett.*, 2019, **44**, 4757.
10 Q. Hu, G. Niu, Z. Zheng, S. Li, Y. Zhang, H. Song, T. Zhai and J. Tang, *Small*, 2019, **15**, 1903496.
11 H. Yu, H. Wang, G. Pozina, C. Yin, X. K. Liu and F. Gao, *Chem. Sci.*, 2020, **11**, 11338–11343.
12 J. Luo, X. Wang, S. Li, J. Liu, Y. Guo, G. Niu, L. Yao, Y. Fu, L. Gao, Q. Dong, C. Zhao, M. Leng, F. Ma, W. Liang, L. Wang, S. Jin, J. Han, L. Zhang, J. Etheridge, J. Wang, Y. Yan, E. H. Sargent and J. Tang, *Nature*, 2018, **563**, 541–545.
13 X. G. Zhao, D. Yang, J. C. Ren, Y. Sun, Z. Xiao and L. Zhang, *Joule*, 2018, **2**, 1662–1673.
14 S. Li, J. Luo, J. Liu and J. Tang, *J. Phys. Chem. Lett.*, 2019, **10**, 1999–2007.
15 S. J. Zelewski, J. M. Urban, A. Surrente, D. K. Maude, A. Kuc, L. Schade, R. D. Johnson, M. Dollmann, P. K. Nayak, H. J. Snaith, P. Radaelli, R. Kudrawiec, R. J. Nicholas, P. Plochocka and M. Baranowski, *J. Mater. Chem. C*, 2019, **7**, 8350–8356.
16 J. Li, J. Duan, X. Yang, Y. Duan, P. Yang and Q. Tang, *Nano Energy*, 2020, **80**, 105526.
17 M. B. Gray, J. D. Majher, T. A. Strom and P. M. Woodward, *Inorg. Chem.*, 2019, **58**, 13403–13410.
18 Z. Xia, Y. Liu, A. Nag and L. Manna, *Angew. Chem., Int. Ed.*, 2021, **60**, 11592–11603.
19 C. Y. Wang, P. Liang, R. J. Xie, Y. Yao, P. Liu, Y. Yang, J. Hu, L. Shao, X. W. Sun, F. Kang and G. Wei, *Chem. Mater.*, 2020, **32**, 7814–7821.
20 D. Cortecchia, J. Yin, A. Petrozza and C. Soci, *J. Mater. Chem. C*, 2019, **7**, 4956–4969.
21 J. Zhou, Z. Xia, M. S. Molokeev, X. Zhang, D. Peng and Q. Liu, *J. Mater. Chem. A*, 2017, **5**, 15031–15037.
22 C. Lv, X. Yang, Z. Shi, L. Wang, L. Sui, Q. Li, J. Qin, K. Liu, Z. Zhang, X. Li, Q. Lou, D. Yang, J. Zang, R. Liu, B. Liu and C.-X. Shan, *J. Phys. Chem. C*, 2019, **124**, 1732–1738.
23 O. Stroyuk, O. Raievska, A. Barabash, M. Batentschuk, A. Osvet, S. Fiedler, U. Resch-Genger, J. Hauch and C. J. Brabec, *J. Mater. Chem. C*, 2022, **10**, 9938–9944.
24 K. S. S. R. T. Williams, *J. Phys. Chem. Solids*, 1990, **51**, 679–716.
25 J. A. Steele, P. Puech, M. Keshavarz, R. Yang, S. Banerjee, E. Debroye, C. W. Kim, H. Yuan, N. H. Heo, J. Vanacken, A. Walsh, J. Hofkens and M. B. J. Roeffaers, *ACS Nano*, 2018, **12**, 8081–8090.
26 W. Paritmongkol, E. R. Powers, N. S. Dahod and W. A. Tisdale, *J. Phys. Chem. Lett.*, 2020, **11**, 8565–8572.
27 Z. Ma, Z. Shi, D. Yang, Y. Li, F. Zhang, L. Wang, X. Chen, D. Wu, Y. Tian, Y. Zhang, L. Zhang, X. Li and C. Shan, *Adv. Mater.*, 2021, **33**, 2001367.
28 D. Manna, J. Kangsabanik, T. K. Das, D. Das, A. Alam and A. Yella, *J. Phys. Chem. Lett.*, 2020, **11**, 2113–2120.
29 Z. Tan, J. Li, C. Zhang, Z. Li, Q. Hu, Z. Xiao, T. Kamiya, H. Hosono, G. Niu, E. Lifshitz, Y. Cheng and J. Tang, *Adv. Funct. Mater.*, 2018, **28**, 1801131.
30 Z. Tan, M. Hu, G. Niu, Q. Hu, J. Li, M. Leng, L. Gao and J. Tang, *Sci. Bull.*, 2019, **64**, 904–909.
31 X. Wang, W. Meng, W. Liao, J. Wang, R. G. Xiong and Y. Yan, *J. Phys. Chem. Lett.*, 2019, **10**, 501–506.
32 K. M. McCall, C. C. Stoumpos, S. S. Kostina, M. G. Kanatzidis and B. W. Wessels, *Chem. Mater.*, 2017, **29**, 4129–4145.
33 S. J. Zelewski, J. M. Urban, A. Surrente, D. K. Maude, A. Kuc, L. Schade, R. D. Johnson, M. Dollmann, P. K. Nayak, H. J. Snaith, P. Radaelli, R. Kudrawiec, R. J. Nicholas,

Published on 02 September 2022. Downloaded by UNIV DEGLI STUDI DI CAGLIARI on 9/21/2022 10:52:37 AM.

P. Plochocka and M. Baranowski, *J. Mater. Chem. C*, 2019, **7**, 8350–8356.

34 K. Thirumal, W. K. Chong, W. Xie, R. Ganguly, S. K. Muduli, M. Sherburne, M. Asta, S. Mhaisalkar, T. C. Sum, H. Sen Soo and N. Mathews, *Chem. Mater.*, 2017, **29**, 3947–3953.

35 S. Li, Z. Shi, F. Zhang, L. Wang, Z. Ma, D. Wu, D. Yang, X. Chen, Y. Tian, Y. Zhang, C. Shan and X. Li, *ACS Appl. Mater. Interfaces*, 2020, **12**, 46330–46339.

36 F. Locardi, E. Sartori, J. Buha, J. Zito, M. Prato, V. Pinchetti, M. L. Zaffalon, M. Ferretti, S. Brovelli, I. Infante, L. De Trizio and L. Manna, *ACS Energy Lett.*, 2019, **4**, 1976–1982.

37 A. Filippetti, C. D. Pemmaraju, S. Sanvito, P. Delugas, D. Puggioni and V. Fiorentini, *Phys. Rev. B: Condens. Matter Mater. Phys.*, 2011, **84**, 195127.

38 W. Gao, C. Ran, J. Xi, B. Jiao, W. Zhang, M. Wu, X. Hou and Z. Wu, *ChemPhysChem*, 2018, **19**, 1696–1700.

39 L. Wang, W. Zheng, F. Vitale, X. Zhang, X. Li, Y. Ji, Z. Liu, O. Ghaebi, C. T. Plass, R. Domes, T. Frosch, G. Soavi, E. Wendler, Y. Zhang and C. Ronning, *Adv. Funct. Mater.*, 2022, **32**, 2111338.

40 L. Lutterotti, S. Matthies and H.-R. Wenk, *Proceeding of the Twelfth International Conference on Textures of Materials (ICOTOM-12)*, 1999, vol. 1, p. 1599.

41 H. Siddique, Z. Xu, X. Li, S. Saeed, W. Liang, X. Wang, C. Gao, R. Dai, Z. Wang and Z. Zhang, *J. Phys. Chem. Lett.*, 2020, **11**, 9572–9578.

42 L. Wang, W. Zheng, F. Vitale, X. Zhang, X. Li, Y. Ji, Z. Liu, O. Ghaebi, C. T. Plass, R. Domes, T. Frosch, G. Soavi, E. Wendler, Y. Zhang and C. Ronning, *Adv. Funct. Mater.*, 2022, **32**, 2111338.

43 L. Zhang, Y. Fang, L. Sui, J. Yan, K. Wang, K. Yuan, W. L. Mao and B. Zou, *ACS Energy Lett.*, 2019, **4**, 2975–2982.

44 W. Meng, X. Wang, Z. Xiao, J. Wang, D. B. Mitzi and Y. Yan, *J. Phys. Chem. Lett.*, 2017, **8**, 2999–3007.

45 J. Luo, S. Li, H. Wu, Y. Zhou, Y. Li, J. Liu, J. Li, K. Li, F. Yi, G. Niu and J. Tang, *ACS Photonics*, 2018, **5**, 398–405.

46 F. Liu, D. Marongiu, R. Pau, V. Sarritzu, Q. Wang, S. Lai, A. G. Lehmann, F. Quochi, M. Saba, A. Mura, G. Bongiovanni, A. Mattoni, C. Caddeo, A. Bosin and A. Filippetti, *EcoMat*, 2020, **2**, e12017.

47 P. Zhang, J. Yang and S. Wei, *J. Mater. Chem. A*, 2018, **6**, 1809–1815.

48 J. Li, Z. Tan, M. Hu, C. Chen, J. Luo, S. Li, L. Gao, Z. Xiao, G. Niu and J. Tang, *Front. Optoelectron.*, 2019, **12**, 352–364.

49 A. Filippetti, S. Kahmann, C. Caddeo, A. Mattoni, M. Saba, A. Bosin and M. A. Loi, *J. Mater. Chem. A*, 2021, **9**, 11812–11826.

50 F. Matusalem, M. Marques, L. K. Teles, A. Filippetti and G. Cappellini, *J. Phys.: Condens. Matter*, 2018, **30**, 365501.

51 S. Lany and A. Zunger, *Phys. Rev. B: Condens. Matter Mater. Phys.*, 2008, **78**, 17–20.

52 A. Simbula, R. Pau, Q. Wang, F. Liu, V. Sarritzu, S. Lai, M. Lodde, F. Mattana, G. Mula, A. Geddo Lehmann, I. D. Spanopoulos, M. G. Kanatzidis, D. Marongiu, F. Quochi, M. Saba, A. Mura and G. Bongiovanni, *Adv. Opt. Mater.*, 2021, **9**, 2100295.

 This journal is © The Royal Society of Chemistry 2022